

Magnetic propulsion of robotic sperms at low-Reynolds number

Islam S. M. Khalil, Ahmet Fatih Tabak, Anke Klingner, and Metin Sitti

Citation: [Applied Physics Letters](#) **109**, 033701 (2016); doi: 10.1063/1.4958737

View online: <http://dx.doi.org/10.1063/1.4958737>

View Table of Contents: <http://scitation.aip.org/content/aip/journal/apl/109/3?ver=pdfcov>

Published by the [AIP Publishing](#)

Articles you may be interested in

[Magnetic resonant wireless power transfer for propulsion of implantable micro-robot](#)

J. Appl. Phys. **117**, 17E712 (2015); 10.1063/1.4918963

[MagnetoSperm: A microrobot that navigates using weak magnetic fields](#)

Appl. Phys. Lett. **104**, 223701 (2014); 10.1063/1.4880035

[Actuation of a robotic fish caudal fin for low reaction torque](#)

Rev. Sci. Instrum. **82**, 075114 (2011); 10.1063/1.3611002

[A basic study of a triangular magnet chain for locomotion control](#)

J. Appl. Phys. **109**, 07E318 (2011); 10.1063/1.3554215

[Bacterial flagella-based propulsion and on/off motion control of microscale objects](#)

Appl. Phys. Lett. **90**, 023902 (2007); 10.1063/1.2431454

A promotional banner for Applied Physics Reviews. On the left is a thumbnail of a journal cover titled 'AIP Applied Physics Reviews' featuring a diagram of a layered structure. The main text reads 'NEW Special Topic Sections' in large white letters. Below this, it says 'NOW ONLINE' in yellow, followed by 'Lithium Niobate Properties and Applications: Reviews of Emerging Trends' in white. The AIP Applied Physics Reviews logo is in the bottom right corner.

NEW Special Topic Sections

NOW ONLINE
Lithium Niobate Properties and Applications:
Reviews of Emerging Trends

AIP Applied Physics
Reviews

Magnetic propulsion of robotic sperms at low-Reynolds number

Islam S. M. Khalil,¹ Ahmet Fatih Tabak,² Anke Klingner,¹ and Metin Sitti²

¹German University in Cairo, New Cairo 11835, Egypt

²Physical Intelligence Department, Max Planck Institute for Intelligent Systems, Stuttgart 70569, Germany

(Received 19 March 2016; accepted 1 July 2016; published online 18 July 2016)

We investigate the microswimming behaviour of robotic sperms in viscous fluids. These robotic sperms are fabricated from polystyrene dissolved in dimethyl formamide and iron-oxide nanoparticles. This composition allows the nanoparticles to be concentrated within the bead of the robotic sperm and provide magnetic dipole, whereas the flexibility of the ultra-thin tail enables flagellated locomotion using magnetic fields in millitesla range. We show that these robotic sperms have similar morphology and swimming behaviour to those of sperm cells. Moreover, we show experimentally that our robotic sperms swim controllably at an average speed of approximately one body length per second (around $125 \mu\text{m s}^{-1}$), and they are relatively faster than the microswimmers that depend on planar wave propulsion in low-Reynolds number fluids. *Published by AIP Publishing.*
[\[http://dx.doi.org/10.1063/1.4958737\]](http://dx.doi.org/10.1063/1.4958737)

Many recent microswimmers are inspired by the locomotion of microorganisms such as peritrichously flagellated *Escherichia coli* and sperm cells. In his lecture entitled *Life at Low Reynolds Number*,¹ Purcell explained the swimming strategies of microorganisms that are based on helical rotation without time-reversal symmetry and with more than one degree of freedom. The complexity of locomotion arises as a consequence of Purcell's scallop theorem, which necessitates nonreciprocal periodic changes in the shape of the swimmer to break time-reversal symmetry. This condition has been achieved in mainly two ways: locomotion using helical traveling waves^{2,3} and planar traveling waves.⁴⁻¹⁰ Alternative ways to realize locomotion in low-Reynolds number have been presented by several research groups through the utilization of magnetically driven,¹¹ self-driven,¹² and microorganism-driven^{13,14} mechanisms. Directional control and maneuvering,² miniaturization and large scale production¹⁵ have been demonstrated within the mentioned approaches. However, it is advantageous, in diverse nanotechnology and biomedical applications, to fabricate functional microswimmers in a single fabrication step (e.g., three-dimensional printing¹⁵) while still being in control of the morphology and geometry. In this letter, we present a facile fabrication technique to provide robotic sperms, as shown in Fig. 1, which resemble the morphology and locomotion of sperm cells in low-Reynolds number fluids, and show by experiments that the locomotion is achieved via nonreciprocal periodic changes in the flexible tail of the robotic sperm.

The fabrication of robotic sperms is done by pumping polymer solution, i.e., polystyrene (168 N, BASF AG) in dimethyl formamide (DMF) and iron-oxide nanoparticles, into a syringe (polymer concentration is 17 wt. % in DMF, weight ratio of iron:polystyrene is 3:2). A strong electric potential of 10 kV is applied between the syringe and a collector, as shown in Fig. 1(a), to draw the solution towards the collector. A syringe pump is used to inject the polymer solution at flow rate of 3 ml/h, and the gap between the syringe needle tip and the collector is adjusted to be 10 cm. The applied electric potential and the distance between the syringe needle and the

collector yield an electric gradient of 100 kV/m. The mentioned electrospinning variables represent a distinct parametric space in which beaded microfibers are likely to appear.¹⁶ For instance, higher or lower input voltages will result in pure fibers or beads, respectively.¹⁷ The robotic sperms are shown in Fig. 1(b). The length of the robotic sperm can be adjusted based on the dimensionless Sperm number¹⁸ $S_p = L(\omega\xi_{\perp}/\mathcal{A})^{1/4}$, where L is the length of the tail, \mathcal{A} is the average bending stiffness of the tail (between $5 \mu\text{m}$ to $10 \mu\text{m}$ in diameter), ω is the rotational velocity, and $\xi_{\perp} \approx 4\pi\eta/(\ln(2L/d) + 0.193)$ is the transverse drag coefficient,⁵ where d is the tail diameter and η is the dynamic viscosity of the fluid (glycerine with viscosity of 0.95 Pa s). The Bending stiffness is approximated from the volume fractions of polystyrene and iron-oxide nanoparticles in the solution, and the average second moment of area of the tail. For instance, optimal Sperm number of 2.1¹⁸ suggests an optimal tail length of $398 \mu\text{m}$ at a rotational frequency of 1 Hz (tail diameter is $2 \mu\text{m}$). The diameter of the filaments can be decreased by increasing the voltage, decreasing polymer concentration, and using reduced concentration.¹⁹ The Sperm number of the robotic sperm in Fig. 1(c) is calculated to be 1.51. Therefore, its propulsive force is not optimal, whereas Fig. 1(d) shows another robotic sperm with Sperm number of 0.43 that will have negligible net displacement based on the scallop theorem, and hence the robotic sperms are cut based on S_p to optimize the propulsive force under the influence of oscillating magnetic field. The cutting process is done manually using micro tweezers. However, Greenfeld and Zussman²⁰ have shown that relatively high strain rate extensional flow of a semidilute polymer solution can result in fragmentation and entanglement loss, and therefore it is possible to fabricate large quantities of robotic sperms using the current technique.

The S_p -based analysis does not account for kinematic and hydrodynamic coupling effects. Therefore, we use full time-dependent resistance matrix in our analysis. The magnetic torque exerted on the magnetic dipole of the robotic sperm results in a deformation and propagation of traveling waves along its flexible tail. The travelling waves are generated by

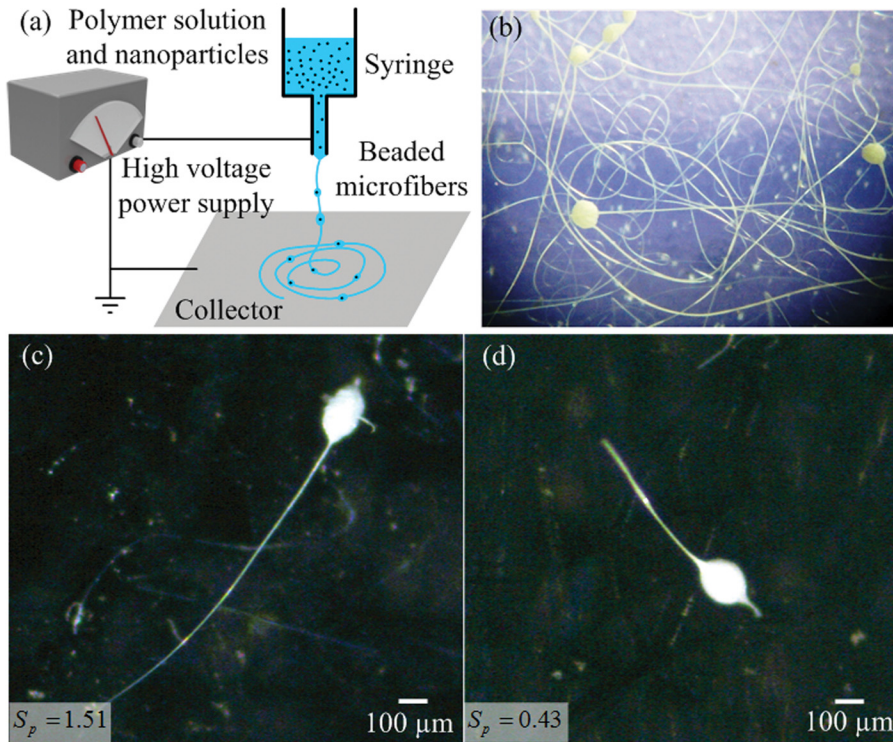


FIG. 1. Fabrication of robotic sperm is realized using polymer solution of polystyrene in dimethyl formamide (DMF) and iron-oxide nanoparticles. (a) A syringe pump injects the polymer solution at controlled flow rate. High electric potential draws the polymer solution towards the grounded collector. (b) Robotic sperm are collected and the iron-oxide nanoparticles are contained within their beads. Conditions: polymer concentration 17 wt. % in DMF, weight ratio iron:polystyrene 3:2, electric field 150 kV/m, and flow rate 1 ml/h. (c) and (d) The sperm number is calculated to be 1.51 and 0.43, respectively.

local bending moment along the tail. This bending moment is generated due to the exerted magnetic torque on the magnetic head of the robotic sperm, and is governed by time-dependent Rayleigh-Timoshenko beam approximation^{21,22}

$$\begin{aligned} & \frac{\partial^2}{\partial x^2} \left(EI \frac{\partial^2 \varphi}{\partial x^2} \right) + f_x \frac{\partial^2 \varphi}{\partial x^2} + (m + m_a) \frac{\partial^2 \varphi}{\partial t^2} + \frac{Jm}{kAG} \frac{\partial^4 \varphi}{\partial t^4} \\ & = f_y + \left(J + \frac{mEI}{kAG} \right) \frac{\partial^4 \varphi}{\partial t^2 \partial x^2} + \frac{J}{kAG} \frac{\partial^2 f_y}{\partial t^2} - \frac{EI}{kAG} \frac{\partial^2 f_y}{\partial x^2}, \quad (1) \end{aligned}$$

where φ is the reference of the structural deformation in the frame of the robotic sperm. Further, G , A , m , and J are the shear modulus, cross-section area, mass per unit length, and moment of inertia per unit length, respectively, and k is the shape correction coefficient for Timoshenko's beam theory. $m_a = \rho V(x)$ is the added mass for the displaced liquid per unit length of the tail, where ρ and $V(x)$ are the density of the medium and the volume of each unit length (dx) along the tail. Furthermore, f_x and f_y are the components of the force (\mathbf{F}_h) exerted on the flexible tail by the surrounding viscous medium

$$\begin{bmatrix} \mathbf{F}_h \\ \mathbf{T}_h \end{bmatrix} = \begin{bmatrix} \mathbf{D}_t + \int_0^L \mathbf{K} d\ell & -\mathbf{D}_t \mathbf{S}_b - \int_0^L \mathbf{K} \mathbf{S}_t d\ell \\ \mathbf{S}_b \mathbf{D}_t + \int_0^L \mathbf{S}_t \mathbf{K} d\ell & \mathbf{D}_r - \int_0^L \mathbf{S}_t \mathbf{K} \mathbf{S}_t d\ell \end{bmatrix} \begin{bmatrix} \mathbf{V} \\ \boldsymbol{\Omega} \end{bmatrix}, \quad (2)$$

where \mathbf{T}_h , \mathbf{V} , and $\boldsymbol{\Omega}$ are the torque exerted by the surrounding viscous medium, linear, and angular rigid-body velocities of the robotic sperm, respectively. \mathbf{D}_t and \mathbf{D}_r are diagonal matrices of translational and rotational resistive force coefficients of the bead of the robotic sperm, respectively. \mathbf{S}_b and \mathbf{S}_t are skew symmetric-matrices signifying the

cross-products for the head and the tail of the robotic sperm, respectively. Further, $\mathbf{K} = \mathbf{RCR}^T$, where $\mathbf{R} = [\mathbf{t} \ \mathbf{n} \ \mathbf{b}]$ is the rotation matrix from local Frenet-Serret coordinate frames to the frame of reference on the center-of-mass of the robotic sperm, where \mathbf{t} , \mathbf{n} , and \mathbf{b} denote respective local tangential, normal and binormal vectors. Further, $\mathbf{C} = \text{diag}(c_t, c_n, c_b)$ is the diagonal matrix of the local resistive force coefficients, where $c_t = 2\pi\eta/(\ln(2L/d) - 0.807)$ and $c_n = c_b = 4\pi\eta/(\ln(2L/d) + 0.193)$. The deformation of the tail is achieved by exerting a magnetic torque using an external source of magnetic field (uniform field along direction of motion and with a sinusoidally varying orthogonal component) with an orthogonal array of electromagnetic coils (the inductance and resistance of each coil are 0.78 H and 5.5 Ω , respectively, and the time-constant is calculated to be 0.14 s). This array surrounds a fluid reservoir that contains the robotic sperm,²³ and the workspace is limited to 4 mm \times 4 mm within the common center of the electromagnetic coils. In addition, the electromagnetic coils provide magnetic fields with almost similar magnitude (18 mT) within a frequency range of 0 Hz to 10 Hz.

Due to the time-dependent deformation, the elements of the full resistance matrix of the robotic sperm in (2) are also calculated in real-time by incorporating fluid resistance in all directions. Therefore, the magnetic field and the hydrodynamic resistance are coupled. Fig. 2 (Multimedia View) shows a representative flagellated swim along negative x -axis at a gradually increasing frequency from 1 Hz to 2 Hz. The robotic sperm swims in glycerine ($\rho = 1260 \text{ kg m}^{-3}$) at average speed of $200 \mu\text{m s}^{-1}$. Therefore, Reynolds number has an order of magnitude of 10^{-6} . We track the position of the bead (red circle) and another point (blue circle) on the tail along x - and y -axis, as shown in Figs. 2(a) and 2(b), respectively. These measurements show the periodic oscillation of the robotic sperm and the nonreciprocal change in shape at the

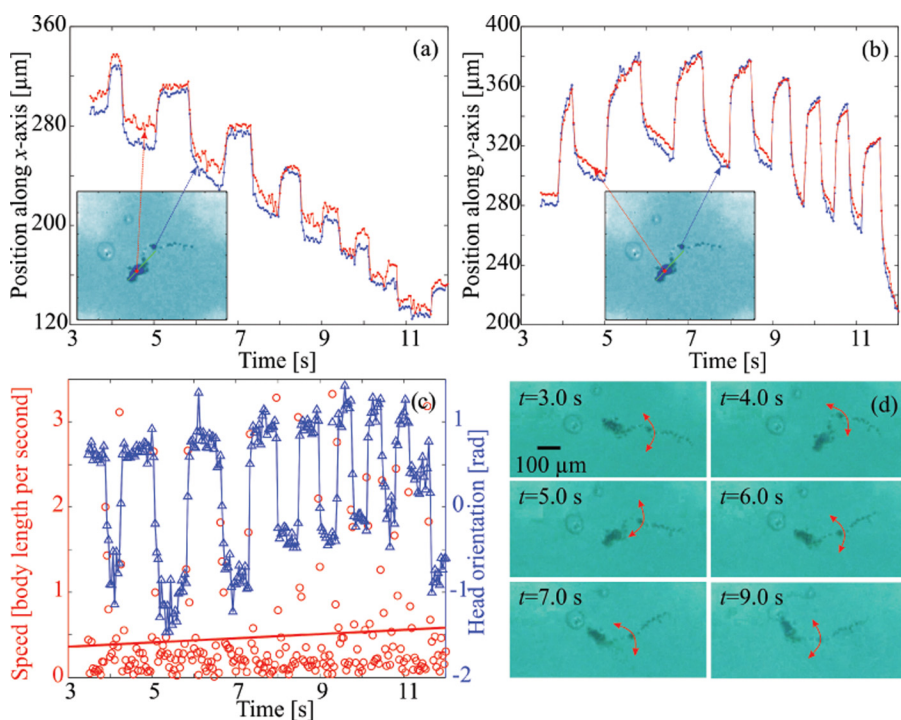


FIG. 2. Locomotion of a robotic sperm is achieved by breaking the time-reversal symmetry using oscillating magnetic fields. (a) and (b) Positions of the head and a representative point on the tail along x - and y -axes versus time. (c) Orientation of the head and its speed. (d) Time-laps of the flagellated locomotion of the robotic sperm. (Multimedia View) [URL: <http://dx.doi.org/10.1063/1.4958737.1>]

point along the tail. The orientation of the magnetic bead (green line) is also measured (Fig. 2(c)) with the speed of the robotic sperm. Locomotion of the robotic sperm is shown in Fig. 2(d). We also calculate the radius of curvature (κ) of the robotic sperm during the flagellated swim to provide comprehensive information of the locomotion, as shown in Fig. 3 (Multimedia view). The curvature is calculated and represented using red curves that are overlaid on the robotic sperm. The curvature has a periodic pattern ($\kappa(t) \approx \kappa(t + \tau)$) which is necessary for the locomotion under the influence of oscillating magnetic field. However, this curvature breaks the time-reversal symmetry. Fig. 3 shows the curvature (blue line) and an overlay of the shifted and time-reversed

curvature (red dashed line) with τ (τ is selected such that best match between curvature and time-reversed curvature is achieved). There exists a considerable deviation between the curves, e.g., at time, $t = 29.6$ s, the curvature $|\kappa| = 2.29 \text{ m}^{-1}$ increases to $|\kappa| = 1.78 \text{ m}^{-1}$ at $t = 29.9$ s. Therefore, the time-reversed curve cannot be overlaid on the original curvature. This experiment is done under the influence of magnetic field of 10 mT at a frequency of 1 Hz. Therefore, the robotic sperm undergoes nonreciprocal periodic changes in its shape, and hence achieves locomotion in low-Reynolds number.

The frequency response is determined experimentally by measuring the average swimming speed from 10 trials at each frequency for 5 different robotic sperms (Fig. 4). We observe

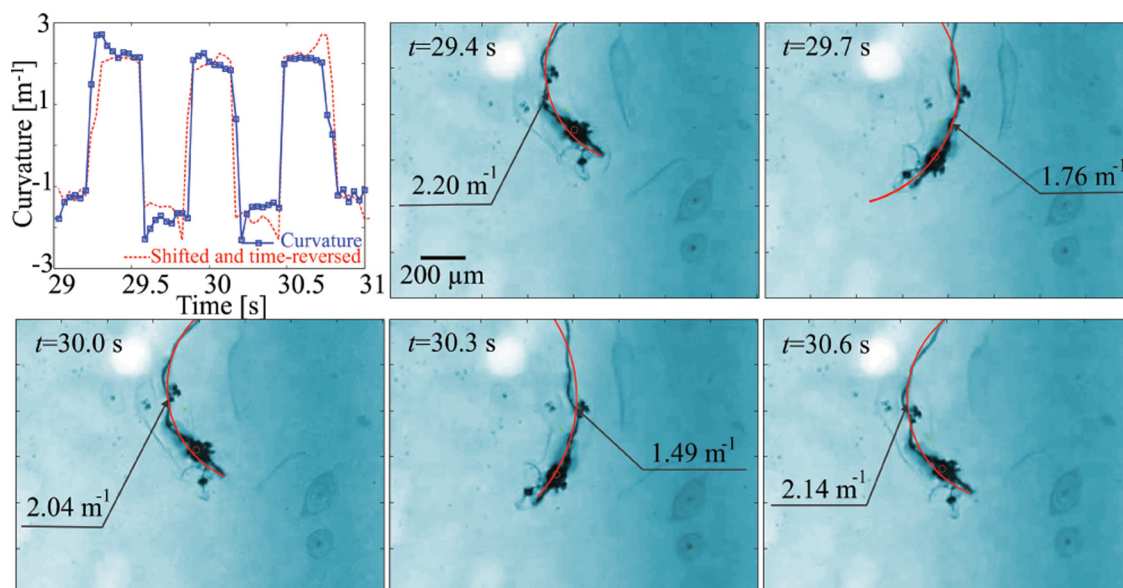


FIG. 3. Curvature of a robotic sperm is calculated at different time-laps to indicate that locomotion is achieved by breaking time-reversal symmetry, at oscillating magnetic field of 1 Hz and 10 mT. The robotic sperm undergoes periodic pattern with nonreciprocal change in shape, $\kappa(t = 29) = -1.78 \text{ m}^{-1} \neq \kappa(t = 30) = 2.04 \text{ m}^{-1} \neq \kappa(t = 31) = -1.09 \text{ m}^{-1}$. (Multimedia View) [URL: <http://dx.doi.org/10.1063/1.4958737.2>]

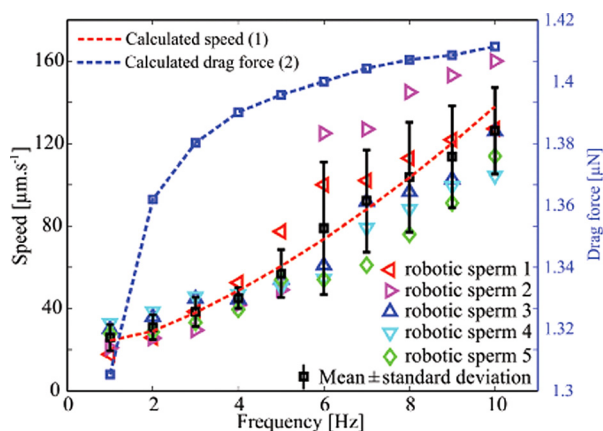


FIG. 4. Measured and calculated average speeds of the robotic sperm. The speed of the robotic sperm increases with the frequency of the oscillating magnetic fields. The magnitude of the drag forces also increases with the speed of the robotic sperm. The measured speed is calculated using 5 different robotic sperm at each frequency.

that the robotic sperm cannot align along the field lines at frequencies higher than 10 Hz (the magnitude of the magnetic field is almost constant within this frequency range). We also observe that the swimming speed decreases at frequencies greater than 10 Hz due to the electric properties (time-constant of the coil is 0.14 s) and the frequency response of the electromagnetic coils. Moreover, the frequency range can be controlled by changing the percentage of the iron-oxide nanoparticles during electrospinning, or changing the electrical properties of the coils. However, increasing the percentage of nanoparticles will have adverse effect on the flexibility of the tail. The calculated speed using the dynamic model (1) is also compared to the measurements and we find good agreement. The drag force exerted on the robotic sperm is calculated at each frequency (Fig. 4) and we observe a non-linear increase with the frequency and the speed of the

robotic sperm. The pull-push-rotate effect of the alternating magnetic field will not yield a controllable net displacement without the structural deformation. However, as the frequency increases, the filament exhibits a time-irreversible deformation pattern which in turn forces the surrounding liquid to push the entire swimmer forward. Fig. 4 is also used to prove that the propulsion of the robotic sperm is due to the flagellated swim and not due to a pulling magnetic force of the electromagnetic configuration. This configuration generates maximum magnetic field gradient of 5 T m^{-1} along the center line of the coil and at the boundary of the workspace, whereas the upper limit on the magnetic dipole moment of the robotic sperm is calculated to be $1.4 \times 10^{-11} \text{ A m}^2$. Therefore, the magnetic force is $7 \times 10^{-11} \text{ N}$. This magnetic force is five orders of magnitude lower than the minimum drag force exerted on a robotic sperm, at the frequency of 1 Hz.

It is likely that the robotic sperm will be used as micro-robots in diverse biomedical and nano-technology applications. Therefore, we show that they controllably swim in two-dimensional space. Two representative motion control trials are shown in Figs. 5(a) and 5(b) (Multimedia view). We devise an experimental control scenario for the robotic sperm by adding two gas bubbles that represent a desired (red dashed circle) and an undesired (blue dashed circle) reference targets. The robotic sperm is required to swim towards the desired reference target, while avoiding the undesired target. Fig. 5(a) shows that the robotic sperm swims at an average speed of $118 \mu\text{m s}^{-1}$ and selectively targets the desired gas bubble at time, $t = 9 \text{ s}$. This representative experiment is done using magnetic field of 14 mT and at the frequency of 4 Hz. Another representative motion control trial is shown in Fig. 5(b) with different initial positions for the robotic sperm and the gas bubbles. The robotic sperm targets the desired gas bubble at time, $t = 8 \text{ s}$, at an average swimming speed of $107 \mu\text{m s}^{-1}$.

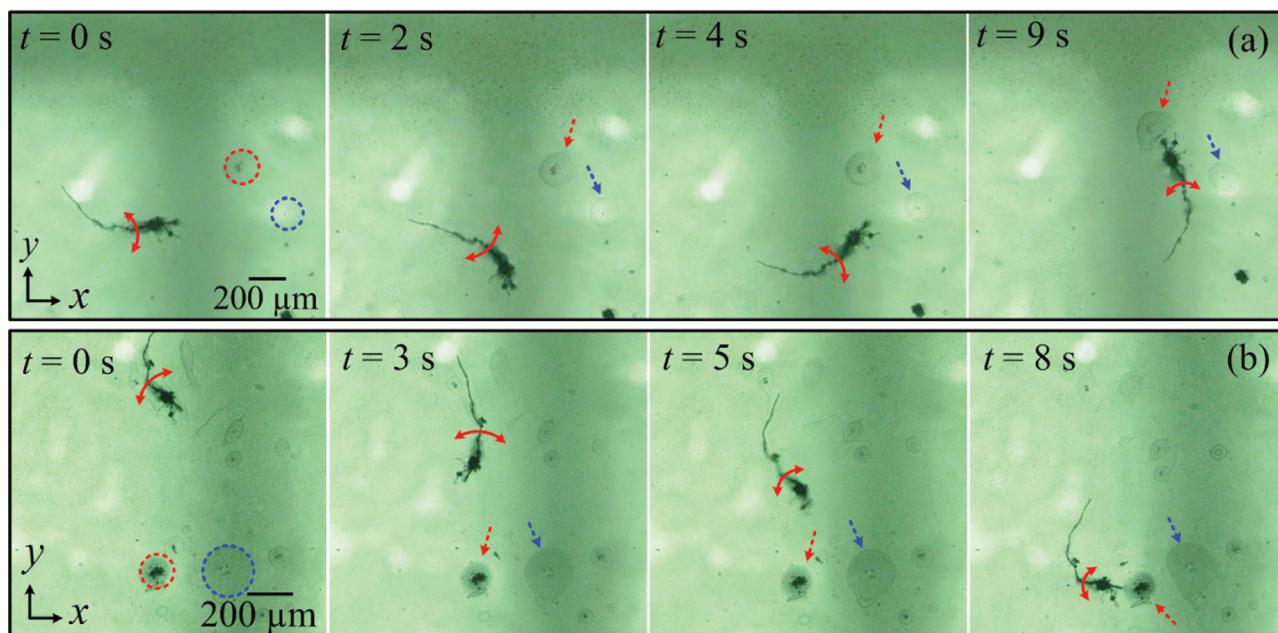


FIG. 5. The robotic sperm swims controllably towards gas bubbles represented using the dashed red circle. The robotic sperm selectively targets the desired bubble and avoid its neighbour indicated by the dashed blue circle. (a) and (b) The robotic sperm swims towards the desired bubble at an average speed of 0.2 body length per second. (Multimedia View) [URL: <http://dx.doi.org/10.1063/1.4958737.3>]

The robotic sperms swim at an average speed of 0.37 ± 0.17 body length per second at frequency of 1 Hz, and maximum swimming speed of 0.99 ± 0.04 body length per second, at the frequency of 10 Hz, whereas the swimming speed of the bull spermatozoon is approximately 1.4 body length per second. Nevertheless, our robotic sperms are relatively faster than their man-made counterparts that depend on planar wave propulsion. The maximum swimming speed of the self-propelled biohybrid swimmer⁶ is 0.083 body length per second. The swimming filament composed of 750 nm particles with the length of $10 \mu\text{m}$ swims at 0.2 body length per second.^{4,24} MagnetoSperm has a maximum swimming speed of 0.49 body length per second.⁷

In conclusion, swimming in low-Reynolds number is achieved by utilizing the flexibility of eletrospun polystyrene microfibers for flagellated propulsion and the dipole moment of iron-oxide nanoparticles for magnetic steering. The fabrication process is relatively flexible and enables production of robotic sperms with similar morphology to that of sperm cells. The robotic sperms are able to swim at an average speed of $125 \mu\text{m s}^{-1}$ (0.9 body length per second) and this speed can be changed by varying the frequency of the external magnetic fields. Furthermore, our model represents the elasto-hydrodynamics and magneto-hydrodynamics of the robotic sperm more accurately, with full time-dependent resistance matrix for the entire robotic sperm, which previous studies did not incorporate.^{25,26} Position control of the robotic sperms is also achieved by selectively targeting gas bubbles as reference targets in the medium to demonstrate their potential future biomedical applications such as targeted therapy and cell manipulation.

The research leading to these results has received funding from the German University in Cairo and the DAAD-BMBF funding project. The authors thank Mr. Abdelrahman Hosney for assistance with the experimental work.

- ¹E. M. Purcell, *Am. J. Phys.* **45**, 3–11 (1977).
- ²A. Ghosh and P. Fischer, *Nano Lett.* **9**, 2243–2245 (2009).
- ³L. Zhang, J. J. Abbott, L. Dong, B. E. Kratochvil, D. Bell, and B. J. Nelson, *Appl. Phys. Lett.* **94**, 064107 (2009).
- ⁴R. Dreyfus, J. Baudry, M. L. Roper, M. Fermigier, H. A. Stone, and J. Bibette, *Nature* **437**, 862–865 (2005).
- ⁵O. S. Pak, W. Gao, J. Wang, and E. Lauga, *Soft Matter* **7**, 8169–8181 (2011).
- ⁶B. J. Williams, S. V. Anand, J. Rajagopalan, and M. T. A. Saif, *Nat. Commun.* **5**, 3081 (2014).
- ⁷I. S. M. Khalil, H. C. Dijkslag, L. Abelmann, and S. Misra, *Appl. Phys. Lett.* **104**, 223701 (2014).
- ⁸Z. Ye, S. Régnier, and M. Sitti, *IEEE Trans. Rob.* **30**, 3–13 (2014).
- ⁹G. Kósa, M. Shoham, and M. Zaaroor, *IEEE Trans. Rob.* **23**, 137–150 (2007).
- ¹⁰E. Diller, J. Zhuang, G. Z. Lum, M. R. Edwards, and M. Sitti, *Appl. Phys. Lett.* **104**, 174101 (2014).
- ¹¹M. P. Kummer, J. J. Abbott, B. E. Kratochvil, R. Borer, A. Sengul, and B. J. Nelson, *IEEE Trans. Rob.* **26**, 1006–1017 (2010).
- ¹²S. Fournier-Bidoz, A. C. Arsenault, I. Manners, and G. A. Ozin, *Chem. Commun.* **4**, 441–443 (2005).
- ¹³B. Behkam and M. Sitti, *Appl. Phys. Lett.* **90**, 023902 (2007).
- ¹⁴V. Magdanz, S. Sanchez, and O. G. Schmidt, *Adv. Mater.* **25**, 6581–6588 (2013).
- ¹⁵M. M. Stanton, C. Trichet-Paredesa, and S. Sánchez, *Lab Chip* **15**, 1634–1637 (2015).
- ¹⁶S. L. Shenoy, W. D. Bates, H. L. Frisch, and G. E. Wnek, *Polymer* **46**, 3372–3384 (2005).
- ¹⁷J. H. Wendorff, S. Agarwal, and A. Greiner, *Electrospinning: Materials, Processing, and Applications*, 1st ed. (Wiley-VCH, 2012).
- ¹⁸E. L. Tony, S. Yu, and A. E. Hosoi, *Phys. Fluids* **18**, 091701 (2006).
- ¹⁹S. Y. Gu and J. Ren, *Macromol. Mater. Eng.* **290**, 1097–1105 (2005).
- ²⁰I. Greenfeld and E. Zussman, *J. Polym. Sci.* **51**, 1377–1391 (2013).
- ²¹T. Kaneko, *J. Phys. D: Appl. Phys.* **8**, 1927–1936 (1975).
- ²²H. E. Rosinger and G. Ritchie, *J. Phys. D: Appl. Phys.* **10**, 1461–1466 (1977).
- ²³I. S. M. Khalil, A. F. Tabak, A. Hosney, A. Mohamed, A. Klingner, M. Ghoneima, and M. Sitti, in *Proceedings of the IEEE International Conference on Robotics and Automation (ICRA)* (Stockholm, Sweden, 2016), pp. 1939–1944.
- ²⁴M. Roper, R. Dreyfus, J. Baudry, M. Fermigier, J. Bibette, and H. A. Stone, *J. Fluid Mech.* **554**, 167–190 (2006).
- ²⁵J. J. Abbott, K. E. Peyer, L. Dong, and B. Nelson, *Int. J. Rob. Res.* **28**, 1434–1447 (2009).
- ²⁶H. Gadêlha, *Regular Chaotic Dyn.* **18**, 75–84 (2013).